

Photometric and Spectroscopic Study of Abell 0671

Zhizheng Pan^{1,2}, Qirong Yuan³, Xu Kong^{1,2*}, Dongxin Fan⁴, Xu Zhou⁵, Xuanbin Lin^{1,2}

¹ Center of Astrophysics, University of Science and Technology of China, Jinzhai Road 96, Hefei 230026, China

² Key Laboratory for Research in Galaxies and Cosmology, USTC, CAS, China

³ Department of Physics, Nanjing Normal University, WenYuan Road 1, Nanjing 210046, China

⁴ Department of physics and Electronics, Guangxi Teachers Education University, Nanning 530001, China

⁵ National Astronomical Observatories, Chinese Academy of Sciences, Datun Road 20A, Beijing 100012, China

Accepted 0000 December 00. Received 0000 December 00; in original form 0000 October 00

ABSTRACT

In this paper we present a photometric and spectroscopic study of the nearby galaxy cluster Abell 0671 (A671) with 15 intermediate-band filters in the Beijing-Arizona-Taiwan-Connecticut (BATC) system and the Sloan Digital Sky Survey (SDSS) data. After a cross-identification between the photometric data obtained from the BATC and SDSS, a list of 985 galaxies down to $V \sim 20.0$ mag in a view field of $58' \times 58'$ is achieved, including 103 spectroscopically confirmed member galaxies. The photometric redshift technique is applied to the galaxy sample for further membership determination. After the color-magnitude relation is taken into account, 97 galaxies brighter than $h_{\text{BATC}} = 19.5$ mag are selected as new member galaxies. Based on the enlarged sample of cluster galaxies, spatial distribution, dynamics of A671 are investigated. The substructures of A671 are well shown by the sample of bright members, but it appears less significant based on the enlarged sample, which is mainly due to larger uncertainties in the light-of-sight velocities of the newly-selected faint members. The SDSS r-band luminosity function of A671 is flat at faint magnitudes, with the faint end slope parameter $\alpha = -1.12$. The SDSS spectra allow us to investigate the star formation history of bright cluster galaxies, and the galaxies in the core region are found to be older than those in the outskirts. No environmental effect is found for metallicities of the early-type galaxies (ETGs). Both mean stellar ages and metallicities in bright member galaxies are found to be correlated strongly with their stellar masses assembled, and such correlations are dependent upon morphology. The positive correlation between age and stellar mass supports the downsizing scenario. By comparing ETG absorption-line indices with the state-of-art stellar population models, we derive the relevant parameters of simple stellar population (such as age, [Fe/H], [Mg/Fe], [C/Fe], [N/Fe], and [Ca/Fe]). The ETGs at cluster center tend to have smaller $H\beta$ indices, indicating that central ETGs are likely to be older. The distribution of total metallicity indicator, $[\text{MgFe}]'$, does not show any environmental effects. The relations between the simple stellar population parameters and velocity dispersion in A671 are in good agreement with previous studies.

Key words: galaxies: clusters: individual (A671) – galaxies: distance and redshifts – galaxies: kinematics and dynamics – galaxies: evolution – methods: data analysis

1 INTRODUCTION

According to the hierarchical scenario of structure formation, massive clusters form by merging small groups continuously and accreting field galaxies along the filament (West et al. 1991, 1995; Colberg et al. 2000). Optical cluster surveys reveal that many galaxy clusters have evidence for dynamically bound substructures (Rhee et al. 1991; Beers et al. 1991). A significant fraction ($\sim 40\%$ – 50%) of clusters show multiple peaks or irregular surface brightness distribution in the X-ray images, indicating that they are still

at dynamically active stage, far from equilibrium (Jones & Forman 1999; Schuecker et al. 2001). Compared with the Einstein-de Sitter case, clusters in early-epoch universe are expected to be more relaxed and less substructured, as supported by many N-body simulation works (Crone et al. 1996; Thomas et al. 1998). The fraction of substructured clusters at different redshifts is thus a useful statistical quantity directly relevant to cosmology. Studies on the dynamics of galaxy clusters thus provide a unique tool to put constraint on the models of cluster formation and evolution.

Dense environment in galaxy clusters should have produced influence on physical properties and evolutionary path for the member galaxies. Previous studies have found that the observational

* E-mail: xkong@ustc.edu.cn

properties of galaxies correlate strongly with local galaxy environment (Gómez et al. 2003; Kauffmann et al. 2004; Baldry et al. 2006). One of the most well-studied relation in galaxy clusters is the morphology-density relation (Dressler 1980; Postman & Geller 1984; Whitmore & Gilmore 1991; Goto et al. 2003; Holden et al. 2007). The core region of a cluster is usually dominated by early-type galaxies (ETGs), while the outer region is dominated by late-type galaxies (LTGs). It is well appreciated that the LTGs gradually lost their gas reservoirs when they were accreted into the core region, and finally evolved into lenticular galaxies (S0). This picture of morphology evolution in galaxy clusters has been supported in high- z morphology-density relation studies (Dressler et al. 1997; Fasano et al. 2000; Smith et al. 2005; Postman et al. 2005). However, it is still uncertain and controversial how local galaxy environment affects star formation histories of cluster galaxies.

The Beijing-Arizona-Taiwan-Connecticut (BATC) system has spent much time in observing a sample of more than 30 nearby ($z < 0.1$) galaxy clusters at different dynamic statuses, aiming at studying their dynamic substructures, luminosity functions, and the star formation properties of cluster galaxies. Abell 0671 (A671; $z=0.0502$) is one target of the BATC galaxy cluster survey. Its Abell richness R is set to be 0 (Abell 1958), with Bautz-Morgan type II-III (Bautz & Morgan 1970). The X-ray emission from the cluster center has been detected by the *Einstein* observatory and the *ROSAT* All-Sky Survey (RASS). The X-ray luminosity of A671 detected in the RASS 0.1-2.4 keV band is $0.9 \times 10^{44} \text{ erg s}^{-1}$, and the X-ray temperature is 3.1 keV (Ebeling et al. 1998), which confirms that this cluster is a relatively poor system. Figure 1 shows the smoothed contours of the *Einstein* X-ray image and the radio map at 1.4 GHz from the NRAO VLA Sky Survey (NVSS), superimposed on the optical image in the BATC- h band. No radio emission is detected at the center of A671. The X-ray surface density contour is quite regular with a single symmetric peak as reported by Jones & Forman (1999). However, the detail structure of A671 is possibly blurred due to the low resolution (~ 1 arcmin spatial resolution) and the large PSF (FWHM ~ 1.5 arcmin) of *Einstein* IPC image. It is easily seen that the X-ray emission peak does not coincide with the central brightest galaxy, IC 2378, with a positional offset of about 90 kpc. A671 is included in the cluster sample of the Wide-field Nearby Galaxy-cluster Survey (WINGS), and two substructures in A671 have been found by Ramella et al. (2007) recently. For a better understanding of the dynamics of A671, it is important to construct a large sample of member galaxies, and the faint galaxies ($18.0 < m_v < 19.5$) should be taken into account. In this paper, we present a multicolor photometry of the galaxies in A671 region with the Beijing-Arizona-Taiwan-Connecticut system. We try to enlarge the sample of cluster galaxies by applying the photometric redshift technique to the spectral energy distributions (SEDs) of the BATC-detected faint galaxies. Based on the SDSS spectra of bright member galaxies, we will derive the star formation histories and chemical abundances, and try to find any clues of environmental effects on the physical parameters of cluster galaxies.

This paper is organized as follows: we present the BATC photometric observations and data reduction in Section 2. In Section 3, we analyze the galaxies with known spectroscopic redshifts in the A671 field. In Section 4, we apply photometric redshift technique to select faint member galaxies in A671. In Section 5, dynamic substructures and luminosity function are investigated based on the enlarged sample of member galaxies. In Section 6, we derive the star formation histories and chemical abundances of the ETGs in A671. Finally, we summarize our work in Section 7. Throughout

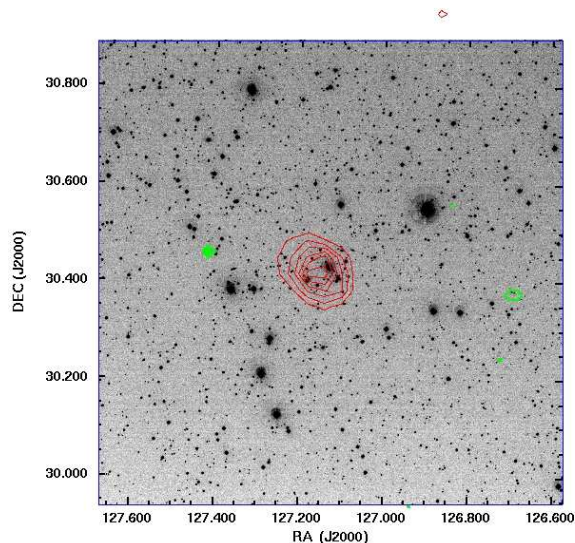


Figure 1. The smoothed contours of *Einstein* image (0.5 – 4.5 keV band) (red line) and the NVSS map at 1.4 GHz (green line), superimposed on the BATC- h band image. The sizes of gaussian smoothing windows are adopted as $30''$ and $1.2'$ for radio and X-ray contours, respectively.

this paper, we assume the cosmological parameters as $\Omega_m = 0.3$, $\Omega_\Lambda = 0.7$, $H_0 = 70 \text{ km s}^{-1} \text{ Mpc}^{-1}$.

2 OBSERVATION AND DATA REDUCTION

The BATC survey is based on the 60/90 cm $f/3$ Schmidt Telescope of National Astronomical Observatories, Chinese Academy of Science (NAOC), located at Xinglong Station. The BATC system contains 15 intermediate-band filters, covering a wavelength from 3000 to 10000 \AA , which are designed to avoid night sky emission lines (Fan et al. 1996; Kong et al. 2000). The transmission curves of BATC filters can be found in Fan et al. (1996). Before October 2006, a Ford CCD camera with a format of 2048×2048 was mounted on the telescope, and photometric observations in 12 bands, from d to p , were carried out. The viewing field was about $58' \times 58'$, with a scale of $1''.7/\text{pixel}$. For pursuing better spatial resolution and higher sensitivity in three blue bands, $a - c$, a new E2V CCD with 4096×4096 pixels was then equipped. The field of view becomes larger ($92' \times 92'$) with a spatial scale of $1''.35/\text{pixel}$. The newly equipped CCD camera has a high quantum efficiency of 92.2%.

From March 2003 to October 2007, we totally accumulated 50 hours exposure for A671 with 15 filters (see the observational information in Table 1). With an automatic data-processing software, PIPELINE I (Fan et al. 1996), we carry out the standard procedures of bias subtraction, flat-field correction, and position calibration. The technique of integral pixel shifting has been used in the image combination during which cosmic rays and bad pixels are removed by comparing multiple images.

For detecting and measuring the flux of the sources within a given aperture in the BATC images, we convert the $a - c$ combined images to make the pixel size identical with $d - p$ images. We adopt a radius of 4 pixels as a photometric aperture for all the BATC images to the sources detected by the *SExtractor* codes (Bertin & Arnouts 1996). The flux calibration of SEDs is performed by using the Oke-Gunn (Gunn & Stryker 1983) stan-

Table 1. The detail of the BATC filters and observation information of A671

Number	Filter name	λ_{eff} (Å)	FWHM (Å)	Exposure (second)	Number of Images	Seeing ^a (arcsec)	Objects Detected	Limiting mag
1	a	3369	222	18000	15	3.79	3945	21.5
2	b	3921	291	7200	6	4.90	4158	21.0
3	c	4205	309	12600	12	4.69	5738	21.0
4	d	4550	332	19500	17	4.61	4739	20.5
5	e	4920	374	15000	14	3.78	5453	20.5
6	f	5270	344	13800	13	4.40	5466	20.0
7	g	5795	289	7800	8	4.12	5506	20.0
8	h	6075	308	7500	7	5.62	5723	20.0
9	i	6660	491	5460	7	3.51	6675	20.0
10	j	7050	238	7500	7	4.14	6017	19.5
11	k	7490	192	12600	12	4.09	5968	19.5
12	m	8020	255	11100	10	4.74	6176	19.0
13	n	8480	167	11100	10	4.24	5893	19.0
14	o	9190	247	15000	14	4.13	5846	18.5
15	p	9745	275	18600	16	4.46	5046	18.5

^a seeing of the combined image

dard stars (HD19445, HD84937, BD+26d2606 and BD+17d4708) which were observed during photometric nights. The detailed information about calibration can be found in Zhou et al. (2001). Because we have no calibration images for *a*, *b*, *c* filters, we instead perform the model calibration that has been developed specially for the large-field photometric system by Zhou et al. (1999). As a result, the SEDs of 6782 sources have been obtained in our catalog. By cross-identifying the BATC sources with the SDSS photometric data within a search circle (defined as a circle of 1.5 arcsec), all sources are classified into galaxies and stars. As a result, 985 galaxies brighter than the BATC-*h* band magnitude limit are found by both surveys, which offers a sample for further analysis.

3 ANALYSIS OF GALAXIES WITH KNOWN SPECTROSCOPIC REDSHIFTS

3.1 Distribution of spectroscopic redshifts

For studying the dynamics of galaxy cluster A671, 205 galaxies with known redshifts in our viewing field are extracted from the SDSS DR8 galaxy catalog. Figure 2 shows the distribution of spectroscopic redshifts of these galaxies. The main concentration with a peak at $z \sim 0.05$ is isolated and less contaminated. There are 103 galaxies with $0.04 < z < 0.06$ and they are selected as the member galaxies of A671, to which we refer as Sample I. To characterize the velocity distribution, we convert the spectroscopic redshifts (z_{sp}) into the rest-frame velocities (v) by $v = c \times (z_{sp} - \bar{z}_c) / (1 + \bar{z}_c)$, where c is the light speed, \bar{z}_c is the cluster redshift with respect to the cosmic background radiation. We take the NED-given cluster redshift $\bar{z}_c = 0.0502$ for A671. The velocity distribution can be fitted by a Gaussian with a dispersion of $\sigma = 625 \text{ km s}^{-1}$, and it is significantly deviated from a standard Gaussian function.

To qualify the distribution of radial velocities of member galaxies, we use the ROSTAT software (Beers et al. 1990) to calculate two resistant and robust estimators, biweight location (C_{BI}) and scale (S_{BI}), analogous to the velocity mean and the standard deviation. For these 103 galaxies, we achieve $C_{BI} = 14561_{-82}^{+100} \text{ km s}^{-1}$, $S_{BI} = 820_{-50}^{+57} \text{ km s}^{-1}$. The errors are determined from the 68% confidence limits based on 10,000 bootstrap resamplings of the velocity data. Taking a cosmological correction factor of

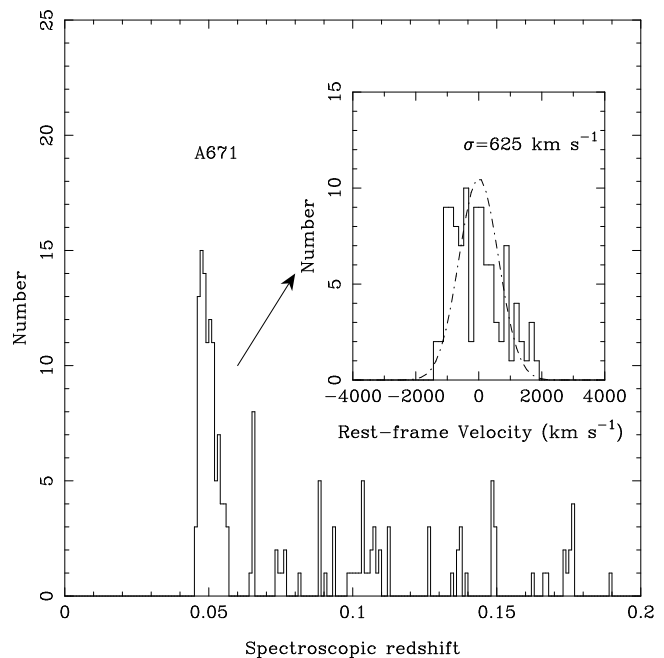


Figure 2. Distribution of the redshifts for 205 galaxies in the A671 field, with bin size $\Delta z = 0.001$. The galaxies in A671 are centered at $z \sim 0.05$. We select the galaxies with $0.04 < z < 0.06$ as member galaxies. The smaller panel shows the distribution of rest-frame velocities of member galaxies in detail, and dash line represents a gaussian fit to the histogram.

$(1 + z)^{-1}$ into account, the velocity dispersion of A671 should be $780_{-47}^{+54} \text{ km s}^{-1}$. Aguerri et al. (2007) studied a sample of 88 nearby clusters. Only 72 galaxies were included in their sample, and a smaller S_{BI} was derived. They found A671 having $C_{BI} = 14599_{-33}^{+19} \text{ km s}^{-1}$ and $S_{BI} = 610_{-33}^{+37} \text{ km s}^{-1}$. Our statistics is based on a larger sample, thus is more reliable. Both studies confirm that A671 has a comparatively small velocity dispersion.

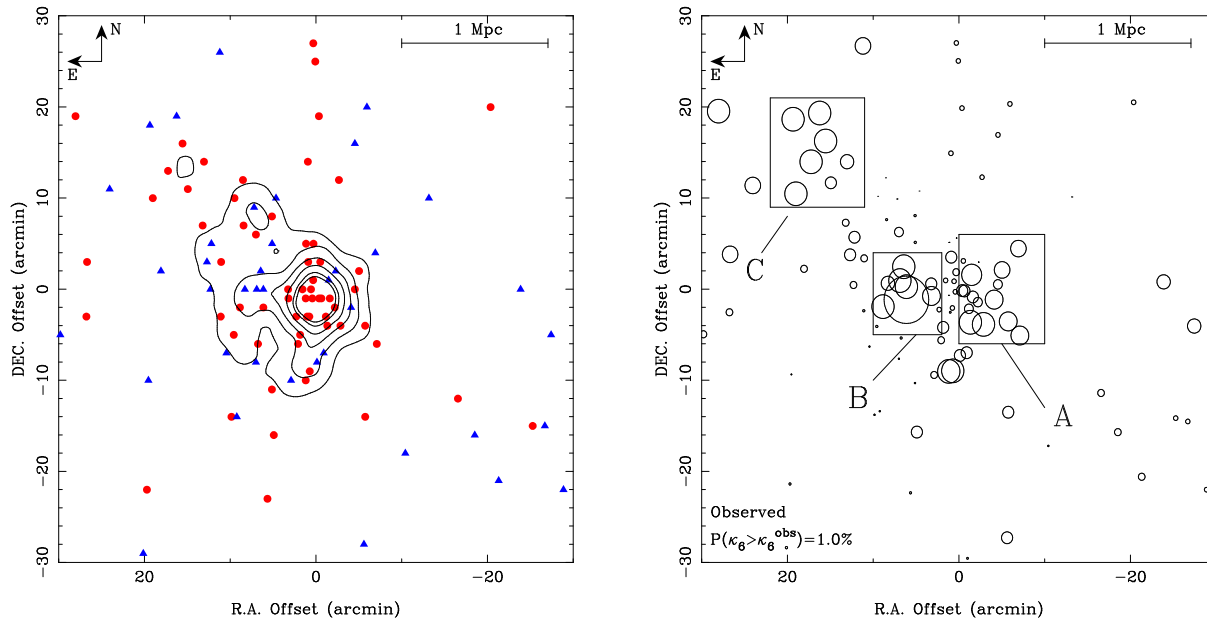


Figure 3. Left: Spatial distribution of 103 known member galaxies of A671, including 63 early-type galaxies (red circles), and 40 late-type galaxies (blue triangles). The contour map of surface density for all these galaxies, smoothed by a Gaussian window with $\sigma = 1.6$ arcmin. The contour levels are 0.09, 0.15, 0.21, 0.27, 0.33 and 0.39 arcmin^{-2} , respectively. Right: Bubble plot for groups of six nearest neighbors, showing the localized variation in velocity distribution.

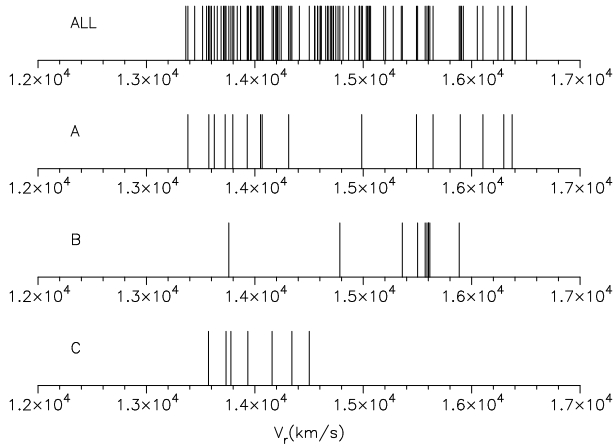


Figure 4. Stripe density plot of velocities of the spectroscopically confirmed galaxies in whole cluster, clumps A, B, and C, respectively.

3.2 Spatial distribution and localized velocity structure

Because A671 is a nearby cluster, our BATC viewing field can not cover whole cluster region. Our photometry focus on a central field of $3.4 \times 3.4 \text{ Mpc}^2$. The radius of galaxy cluster, r_{200} , is defined in former studies as the boundary of a cluster, within which the mean inner density is $200\rho_c$, where ρ_c is the critical density of the Universe (Gott 1972). We calculate the r_{200} for A671 following the formula suggested by Carlberg et al. (1997). The r_{200} is a function of velocity dispersion. By applying the S_{BI} we derived, the r_{200} of A671 is 2.25 Mpc, corresponding a slightly larger area than our viewing field.

Before studying the dynamic structure of A671, we try to classify the 103 known members into ETGs and LTGs. The early-type members should meet two requirements: (1) with no evident emission lines; (2) with no evident galaxy arms. We firstly extract

those galaxies with $\text{EW}(\text{H}\alpha) < 5 \text{ \AA}$ as early-type candidates. The $\text{EW}(\text{H}\alpha)$ values are taken from the MPA/JHU catalog¹ of SDSS galaxies. Then we inspect their SDSS-given images and removing those with arms. As a result, the 103 galaxies are classified into 63 ETGs and 40 LTGs.

The left panel of Figure 3 presents the spatial distribution of 103 known member galaxies within our field of view, with the central position of A671, $\text{R.A.} = 8^{\text{h}}28^{\text{m}}29^{\text{s}}$, $\text{Dec.} = 30^{\circ}25'01''$ (for the J2000 equinox). We superpose the contour map of surface density that has been smoothed by a Gaussian window with $\sigma = 1.6'$. As shown in Figure 3, the member galaxies are mainly concentrated in the central region within a radius of 1 Mpc. The irregular contour in the east and north corresponds to the two substructures found by Ramella et al. (2007). More statistical tests should be performed before we can reach a firm conclusion that there are substructures in A671.

To show the substructures of A671 in both velocity space and projected map, we make use of the κ -test (Colless & Dunn 1996) for the 103 galaxies. The statistic variable, κ_n , is defined to quantify the local deviation on the scale of groups of n nearest neighbors. A larger κ_n indicates a greater probability that the local velocity distribution differs from overall velocity distribution. The probability $P(\kappa_n > \kappa_n^{\text{obs}})$ can be calculated by Monte Carlo simulations with random shuffling velocities. When the scale of the nearest neighbors n varies from 3 to 9, the probabilities $P(\kappa_n > \kappa_n^{\text{obs}})$ are nearly zero, which means the substructure appears very obvious at different scales. The bubble plot at the scale of $n = 6$ is given in the right panel of Figure 3. Since the bubble size is proportional to $-\log P(D_n > D_n^{\text{obs}})$, the clustering of large bubbles is a good tracer of dynamical substructure.

As we can see in the bubble plot, the central region of A671 is dominated by two clumps of bubbles, and a clump of large bubbles

¹ <http://www.mpa-garching.mpg.de/SDSS/DR7>

in the north-east is also remarkable. We refer to these three clumps as A, B, and C, which contain 16, 10, 8 galaxies, respectively. For confirming whether these clumps trace the real substructures, we present the velocity distributions for subsamples A, B, and C in Figure 4, as well as the velocity distribution of the whole sample. It is easily seen that the velocity distributions for the three clumps are indeed deviated from that of the whole sample. The mean velocities of the subsamples A, B, and C are 14638^{+408}_{-641} , 15567^{+23}_{-266} , and 13992^{+171}_{-174} km s⁻¹, respectively. The mean velocities of subsamples B and C are significantly deviated from the mean velocity of the whole sample, 14561 km s⁻¹. Though the mean velocity in clump A is similar to that of the whole sample, the galaxies in clump A have a remarkable bimodal velocity distribution, which may imply the existence of two different groups. To quantify the bimodality significance, we apply the Gaussian mixture modeling (GMM) method (Muratov & Gnedin 2010) to the velocity distribution for clump A. The result shows that clump A consists of two components, which peaked at 13829 km s⁻¹ and 15824 km s⁻¹. The unimodal velocity distribution can be rejected at 99% significance level.

Although the velocity distribution of the subsamples are significantly deviated from the whole sample, their masses should also be large enough if they are real substructures. The masses of the A671 and its clumps can be estimated by applying the virial theorem. Assuming that each subcluster is bound and the galaxy orbits are random, the virial mass (M_v) can be derived from the following standard formula (Geller & Peebles 1973; Oegerle & Hill 1994):

$$M_v = \frac{3\pi}{G} \sigma_r^2 D N_p \left(\sum_{i>j} \frac{1}{\theta_{ij}} \right)^{-1}, \quad (1)$$

where σ_r is the light-of-sight velocity dispersion, D is the cosmological distance of the cluster, $N_p = N(N-1)/2$ is the number of galaxy pairs, and θ_{ij} is the angular distance between galaxies i and j . The virial masses of A671 is $9.49 \times 10^{14} M_\odot$. Clump B is the most remarkable among the 3 subsamples, with virial mass of $1.53 \times 10^{14} M_\odot$. The A clump consists of two groups, with virial mass of $\sim 7.0 \times 10^{13} M_\odot$ for each. Clump C has similar virial mass. Thus we conclude that A671 is not a simple relaxed cluster, but most likely at a dynamically active stage.

4 SED SELECTION OF FAINT CLUSTER GALAXIES

The technique of photometric redshift can be used to estimate the redshifts of galaxies by using the SED information covering a wide range of wavelength instead of spectroscopy. This technique has been extensively applied to the multicolor photometric surveys for detecting the faint and distant galaxies, and for subsequent selection of cluster galaxies (Fernández-Soto et al. 1999; Ilbert et al. 2009; Kong et al. 2009). Based on the standard SED-fitting code called *HyperZ* (Bolzonella, Miralles & Pelló 2000), for a given object, the photometric redshift, z_{ph} , corresponds to the best fit (in the χ^2 -sense) of its photometric SED with the template SED generated by convolving the galaxy spectra in the template library with the transmission curves of specified filters. Previous work has demonstrated the accuracy of photometric redshift with the BATC multicolor photometric data (Xia et al. 2002; Yang et al. 2004; Liu et al. 2011; Zhang et al. 2011). In our SED fitting, only normal galaxies are taken into account in the reference templates. Dust extinction with a reddening law of the Milky Way (Allen 1976) is adopted, and A_V is allowed to be flexible in a range from

0.0 to 0.5, with a step of 0.05. The photometric redshift of a given galaxy is searched from 0.0 to 0.6, with a step of 0.005. We apply this technique to all BATC galaxies brighter than $h_{\text{BATC}} = 19^m.5$. The procedure of SED-fitting has provided the best-fit photometric redshift and its uncertainty for each galaxy.

From the 205 galaxies with known spectroscopic redshifts (z_{sp}), we select 167 galaxies (including 91 member galaxies) that are simultaneously detected in at least 12 BATC bands to derive their z_{ph} values. A comparison between z_{ph} and z_{sp} values is shown in the top-left panel of Figure 5. The error bar of z_{ph} corresponds to 68% confidence level in photometric redshift determination. The solid line denotes $z_{\text{ph}} = z_{\text{sp}}$, and the dashed lines show an average redshift deviation of $0.02(1+z)$. It is obvious that our z_{ph} estimates are basically consistent with their z_{sp} values. For 91 member galaxies in our spectroscopic sample, the mean value and standard deviation of their z_{ph} values are 0.0505 and 0.0112, respectively. There is no systematic offset in the z_{ph} domain with respect to the z_{sp} distribution. Statistically, 85 member galaxies (about 93 percent) are found to have their photometric redshifts within $\pm 2\sigma$ deviation, in a range from 0.028 to 0.073, demonstrating the robustness of our z_{ph} estimate. This z_{ph} region can be applied as a selection criterion in the following membership determination for faint galaxies.

The top-right panel of Figure 5 shows the histogram of photometric redshifts for all galaxies down to $h_{\text{BATC}} = 19^m.5$. The black histogram shows z_{ph} distribution for the 167 galaxies with known spectroscopic redshifts mentioned above. As expected, the peak in the z_{ph} distribution is around $z=0.05$. In the bottom-left panel of Figure 5, we show the z_{ph} uncertainties for these 167 galaxies as a function of BATC- h band magnitude. It is remarkable that the z_{ph} deviation of fainter galaxies tends to be larger. For the faint galaxies with $h_{\text{BATC}} = 18^m.0$, our z_{ph} estimate is still robust, but with larger uncertainty. For the remainder galaxies without z_{sp} values, we give a plot of their z_{ph} uncertainties versus BATC- h band magnitudes in the bottom-right panel in Figure 5. The larger z_{ph} uncertainties for faint galaxies are mainly due to larger magnitude errors in photometry. For a reliable membership determination based on the z_{ph} estimate, we exclude the galaxies fainter than $h_{\text{BATC}} = 19^m.5$, and take the galaxies with $0.028 < z_{\text{ph}} < 0.073$ as member candidates. Due to the robustness of our photometric redshift technique, it is conservative that our selecting criterion would be able to select 80-90% of faint members with least contaminants.

It is well known that there exists a correlation between color and absolute magnitude for the ETGs (C-M relation) (Bower et al. 1992), in the sense that brighter ETGs appear redder, which can be used for verifying the membership selection of the ETGs. The left panel of Figure 6 presents the correlation between the color index, $b-h$, and BATC- h band magnitude for the whole member candidates down to $h_{\text{BATC}} = 19^m.5$, while the right panel shows the SDSS color index, $g-r$, and r -band magnitude. The diagrams include the following categories of sources: (1) spectroscopically confirmed early-type member candidates (denoted by filled circles), (2) spectroscopically confirmed late-type member candidates (denoted by filled triangles), (3) newly-selected faint member candidates (denoted by open triangles). The solid line represents the linear fitting with the 63 spectroscopically confirmed ETGs: $b-h = -0.09(\pm 0.02)h + 3.47(\pm 0.43)$, and the dashed line represents 1σ deviation. The linear fit of the ETGs in the right panel of Figure 6 is $g-r = -0.026(\pm 0.006)r + 1.21(\pm 0.10)$. As shown in both figures, the early-type member galaxies follow a very tight color-magnitude relation, faint member candidates also

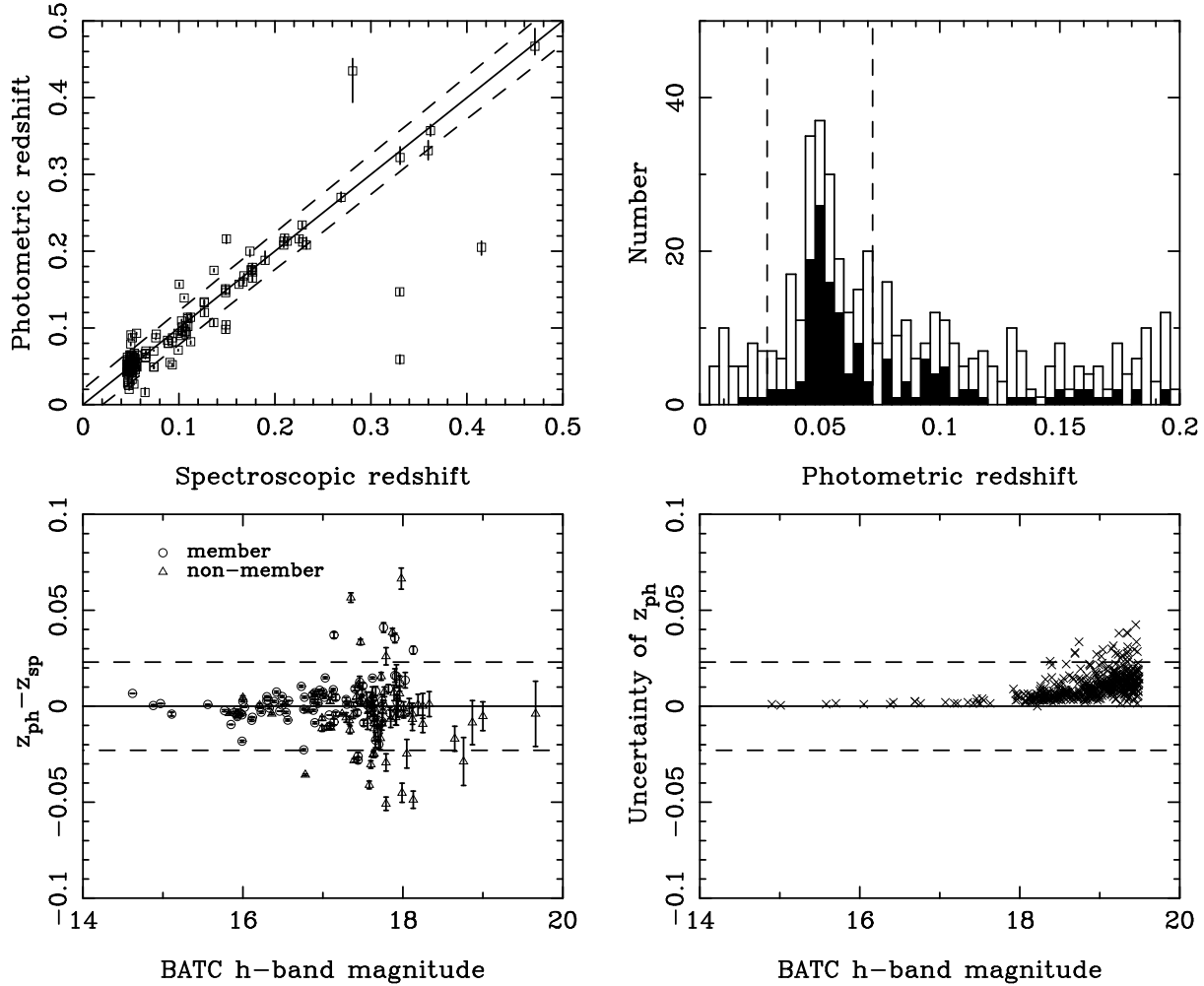


Figure 5. Top-left: comparison between z_{ph} and z_{sp} 167 galaxies detected with at least 12 BATC bands. The error bars shows the 68% significance coefficient level. Solid line denotes $z_{\text{ph}} = z_{\text{sp}}$, and the dash lines denote the deviation of $0.02(1+z)$. There is no systematic deviation between the photometric redshifts and the spectroscopic redshifts. Top-right: z_{ph} distribution for the galaxies down to $h_{\text{BATC}} = 19^m.5$, with a bin size of $\Delta z = 0.004$. The black histogram shows the z_{ph} of the 167 galaxies with z_{sp} . The dash line shows our faint member candidates selection criterion. Bottom-left: difference of z_{ph} and z_{sp} for the 167 galaxies with spectroscopic redshifts. Circles denote member-galaxies, and triangles denote non-members. The dash lines denote the member selection criteria ($2\sigma = 0.023$). The error bars are given by the *HyperZ* codes, with 68% confidence level. Bottom-right: crosses denote 1σ errors of the of the z_{ph} for the left galaxies with h-band magnitude brighter than 19.5 mag in the viewfield of A671.

follow the same C-M relation basically, but seem to be more scattered. This might be caused by some high- z galaxies that have been mixed into our faint member candidates. For excluding these contaminants, we utilize the SDSS C-M relation, and remove the ETG candidates with color indices $g - r$ 0.15 mag redder than the red sequence denoted by the black solid line.

Finally, we obtain a list of 97 newly-selected member galaxies. Combined with those 103 spectroscopically confirmed members, we form an enlarged sample of 200 galaxies in A671, to which we refer as Sample II in following investigation.

5 THE PHYSICAL PROPERTIES OF A671

5.1 The Spatial Distribution and Velocity Structure

The left panel of Figure 7 shows the projected positions of the galaxies in Sample II, superposed with the contour map of surface density smoothed by a Gaussian window with $\sigma = 1.6'$. The

103 member galaxies with known spectroscopic redshifts are denoted by filled symbols, and 97 photometrically selected galaxies are denoted by open symbols. Red symbols represent the early-type member galaxies and blue symbols represent late-type ones. Our BATC multicolor photometry facilitates the finding of large number of faint member galaxies, and makes the underlying substructure along north-east direction more remarkable. Basically, the distribution of faint galaxies traces that of bright ones, and no significant substructures are found with Sample II.

The morphology segregation becomes more remarkable in Sample II. Both bright and faint ETGs are highly concentrated in the core region, while the LTGs are scattered in the outskirts. The shape of contour map seems in accord with the X-ray image, which might demonstrate the reliability of our membership selection based on the BATC multicolor photometry.

For detecting the potential substructures in A671, we perform the κ -test for Sample II. The right panel of Figure 7 shows the bubble plot that characterizes the degree of difference between the localized velocity distribution, for groups of six nearest neighbors,

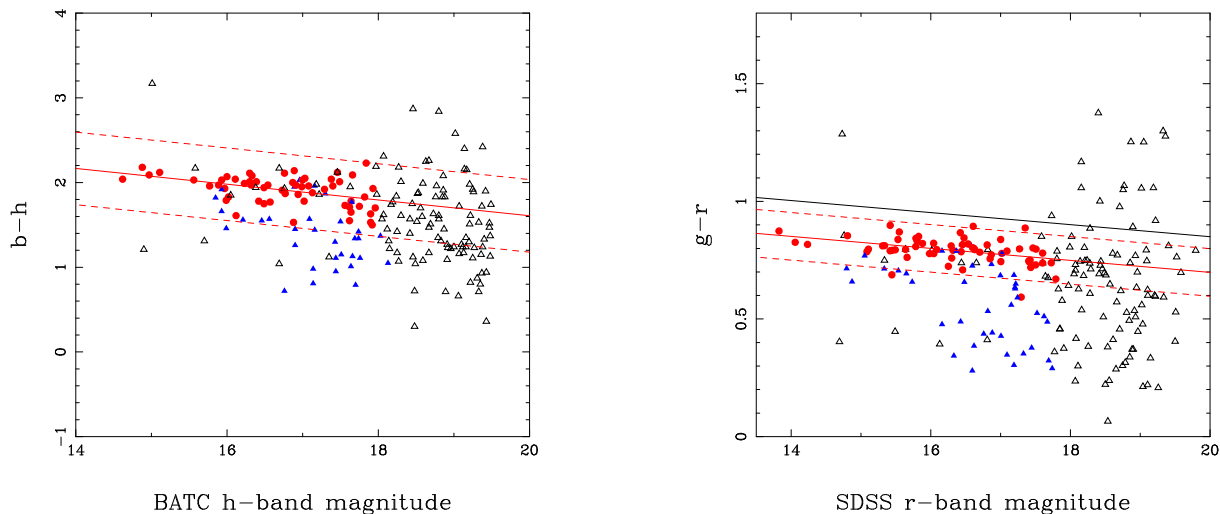


Figure 6. The left panel shows the BATC C-M relation, using color index $b - h$ and h -band magnitude, for the spectroscopically confirmed members and the galaxies with $0.028 < z_{\text{ph}} < 0.073$. The right panel shows the SDSS C-M relation, using color index $g - r$ and SDSS r -band model magnitude. The filled red circles denote the spectroscopically confirmed ETGs in A671. The filled triangles denote the spectroscopically confirmed LTGs in A671. The open triangles denote the newly selected galaxies with $0.028 < z_{\text{ph}} < 0.073$. The solid red lines represent the subsequence fitted with the known early-type members. The dashed red lines represent the 1σ of the best-fit C-M relations. The black solid line represents our selection criterium based on the SDSS C-M relation.

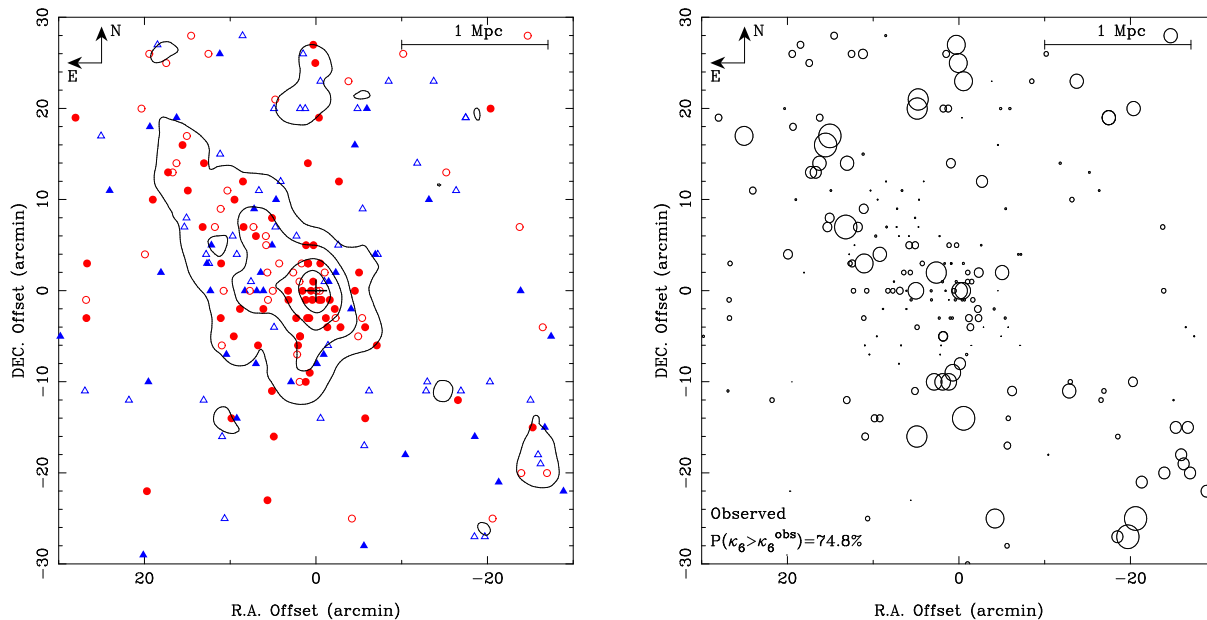


Figure 7. Left: spatial distribution of all member galaxies in Sample II. Filled symbols denote the galaxies with known spectroscopic redshifts, while open symbols represent newly selected members. Red circles denote red-sequence galaxies, while blue open triangles denote those below 1σ of the red-sequence. Right: bubble map shows the local velocity distribution for groups of six nearest neighbors for the whole member galaxies.

and the overall velocity distribution. We performed 10^3 simulations to estimate probability $P(\kappa_n > \kappa_n^{\text{obs}})$ for different group sizes. The probability is found to be more than 5% in all cases, which means that no substructure is detected at 2σ significance (see Table 2). This is not consistent with the conclusion that we have achieved based on Sample I. We think that the substructure unveiled by the spectroscopic redshifts is surely true. Above inconsistency can be well interpreted that the velocities derived from the z_{ph} estimates are not accurate enough to reflect the subtle velocity structure. The abnormality in velocity distribution of substructures might have been

smoothed/swept by the z_{ph} uncertainties of 97 newly selected faint galaxies. So the κ -test on Sample II might be misleading. Follow-up spectroscopy of these faint member galaxies are needed if one wants to investigate the substructures in A671 in detail.

5.2 The Luminosity Function

The luminosity function (LF) is a key diagnostic for clusters because it is tightly related to dynamical evolution and merging history of galaxy clusters. The LF has been widely studied in the

Table 2. Result of the κ -test for member galaxies

Neighbors size (n)	$P(\kappa_n > \kappa_n^{\text{obs}})$ Sample I	$P(\kappa_n > \kappa_n^{\text{obs}})$ Sample II
3	1.4%	34.7%
4	0.6%	35.9%
5	2.8%	65.3%
6	1.0%	74.8%
7	0.5%	71.5%
8	0.7%	65.7%
9	1.4%	62.0%

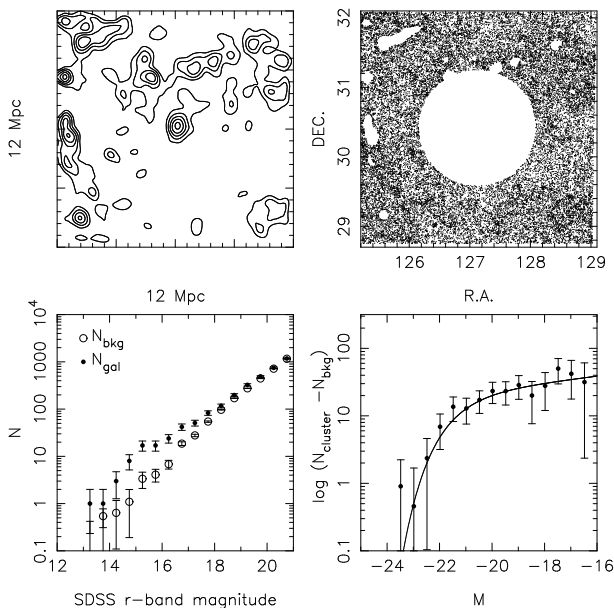


Figure 8. Top left: Density map of a 12×12 Mpc region around A671. Contour levels are from 1σ to 5σ , spaced 1σ apart. Top right: The region which is used to estimate the local background. Dots denote the galaxies with the SDSS r-band magnitude brighter than 21.0 mag. Empty regions represent the removed overdensity area. Bottom left: galaxy number counts extracted within $r=1.7$ Mpc region (filled circles), and those in the local background (open circles) for A671. Bottom right: background-subtracted number counts for A671. The solid line represents the best-fit Schechter function.

past decades and it is well described by the Schechter function (Schechter 1976):

$$\phi(L)dL = \phi^* (L/L^*)^\alpha \exp(-L/L^*) d(L/L^*), \quad (2)$$

where ϕ^* , L^* , and α are the normalization parameter, the characteristic luminosity, and the slope parameter at faint end, respectively. In the domain of absolute magnitude, the Schechter function can be expressed as:

$$\phi(M)dM = \phi^* 10^{0.4(\alpha+1)(M^*-M)} \exp[-10^{0.4(M^*-M)}] dM, \quad (3)$$

where M^* is the characteristic absolute magnitude.

The most challenging issue in measuring the LFs of galaxy clusters (GCs) is that one needs to pick up cluster members out of background galaxies along the line of sight. Ideally, one needs the spectroscopic redshifts for all galaxies to exclude non-members in the cluster field. Unfortunately spectroscopic measurements are rather time-consuming. Our BATC photometry enables us to se-

lect a set of cluster member candidates by utilizing the photometric redshift technique. As seen in Figure 5, the accuracy of z_{ph} is a function of galaxy apparent magnitude. Further corrections are still needed to remove the contribution of contaminant sources and compensate the missing members when investigating the LFs. Unfortunately the exact form of the correction function, particularly at the faint magnitudes, is very difficult to be derived.

Using the SDSS r-band photometric data, we perform the statistical background subtraction to estimate the contribution of non-members to the number counts of galaxies in the cluster direction, by measuring the projected number counts of field galaxies outside the cluster region. The background is estimated with a 12×12 Mpc region centered on the cluster centroid, outside the cluster region defined by a radius of 3 Mpc, where the contamination from cluster galaxies should be negligible. Following the method of Paolillo et al. (2001), we firstly generate a density map of galaxies in the background region by convolving the projected distribution of galaxies with a Gaussian kernel of $\sigma=250$ kpc in the cluster rest frame (the typical size of a cluster core). Then we mask out all density peaks which are above 3σ level from the background region. Masked-out regions covered about 3.3% of the whole background area. Finally we calculate the number counts from the remain galaxies to estimate the background number counts in the cluster direction.

Recent studies have provided evidences that the LFs of GCs do vary with clustercentric radius (Beijersbergen et al. 2002; Hansen et al. 2005). A suitable region should be chosen which is large enough to contain most member galaxies and do not include much projected contamination. We adopt a aperture of $r=30'$ centered at the cluster centroid (about 1.7 Mpc at the rest frame of A671). The results of the background estimation and final luminosity function are showed in Figure 8. The apparent magnitudes are converted to absolute magnitudes by the relation

$$M = m - DM(z) - K_{0.1}(z) \quad (4)$$

Where $DM(z)$ is the distance modulus as determined from the redshift assuming a particular cosmology. $K_{0.1}(z)$ is the K -correction from a galaxy at z to $z = 0.1$. We estimate the $K_{0.1}(z)$ using the software KCORRECT(version 4.1-4, Blanton et al. (2003)). As showed in the bottom-right panel of Figure 8, a single Schechter function can fit the data very well. The best fit parameters are $\phi^*=21.0$, $M^*=-21.6$, $\alpha=-1.12$, which is in good agreement with de Filippis et al. (2011). No strong ‘‘upturn’’ at faint magnitudes is observed for A671.

6 STAR FORMATION HISTORY AND ELEMENT ABUNDANCES

As mentioned in the first section, many former studies support that galaxy properties strongly correlate with local environment. The remarkable morphology-segregation of A671 demonstrates that the morphologies of member galaxies strongly correlate with their local environment. In this section we would like to investigate the star formation histories (SFHs) of the confirmed member galaxies by applying models of stellar population synthesis on their observed spectra. Two models will be taken in this section. On the one hand, we fit the SDSS spectra by the STARLIGHT² code (Cid Fernandes et al. 2005; Mateus et al.

² www.starlight.ufsc.br

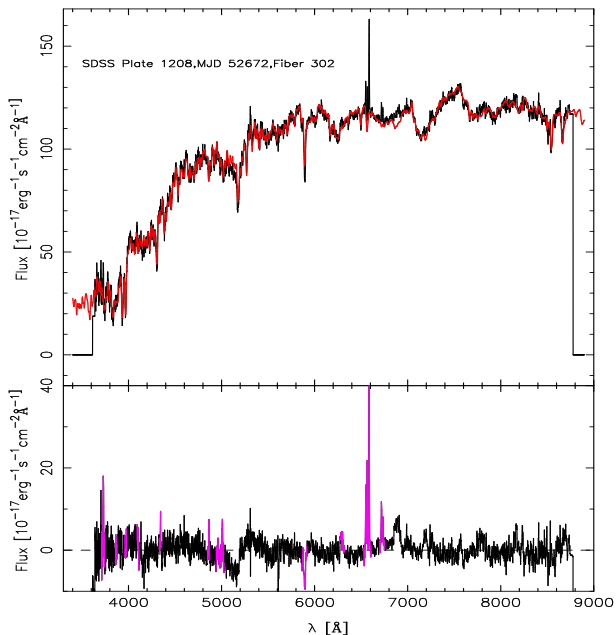


Figure 9. Spectral synthesis of the brightest galaxies in A671. Top panel shows the observed spectrum (black line) and model spectrum (red line). Bottom panel shows the residual spectrum (black line) and the mask regions (pink lines).

2006; Cid Fernandes et al. 2007) to derive the physical parameters based on their SFHs. On the other hand, we compare the absorption line indices (the Lick/IDS indices) of the member ETGs with the model predictions developed by Shiavon (2007) (hereafter S07) to put constraints on the SFHs and chemical enrichment.

6.1 Fitting Spectra with STARLIGHT

We fit the SDSS spectra of member galaxies with the STARLIGHT codes, which aims at fitting an observed spectra with a linear combination of theoretical simple stellar populations (SSPs). The model spectrum is given by

$$M_{\lambda} = M_{\lambda_0} \left(\sum_{j=1}^N x_j b_{j,\lambda} r_{\lambda} \right) \otimes G(v_*, \sigma_*), \quad (5)$$

where M_{λ} is the model spectrum, M_{λ_0} is the synthesis flux at the normalization wavelength λ_0 , x_j is the so-called population vector, $b_{j,\lambda}$ is the j th SSP spectrum at λ , and $r_{\lambda} \equiv 10^{-0.4(A_{\lambda} - A_{\lambda_0})}$ represents the reddening term. The $G(v_*, \sigma_*)$ is the line-of-sight stellar motions that modelled by a Gaussian distribution centered at velocity v_* and with a dispersion of σ_* . N is the total number of SSP models. In our work, the SSP base is made up of $N = 45$ SSPs, three metallicities ($Z = 0.2Z_{\odot}, Z_{\odot}, 2.5Z_{\odot}$) and 15 ages (from 1 Myr to 13 Gyr), which are taken from evolutionary models in Bruzual & Charlot (2003). The galactic extinction law of Cardelli, Clayton & Mathis (1989) with $R_V = 3.1$ is adopted.

All SDSS observed spectra are shifted to the rest-frame, and then interpolated into a resolution of 1 Å before fitting. Wavelength regions of emission lines are masked out. Figure 9 shows the spectral fitting for the brightest cluster galaxy (BCG) of A671. As demonstrated by this figure, the combination of SSP spectra can fit the observed spectrum very well.

The STARLIGHT presents the SSP fraction, intrinsic extinction A_V , velocity dispersion σ , and stellar mass M_* . Following Cid Fernandes et al. (2005), we derive the flux- and mass-weighted average ages, which are defined as

$$\langle \log t_* \rangle_L = \sum_{j=1}^N x_j \log t_j; \quad \langle \log t_* \rangle_M = \sum_{j=1}^N u_j \log t_j, \quad (6)$$

where x_j is the flux-weighted population vector (i.e., the fraction of flux contributed by certain SSP), and u_j is the mass-weighted population vector. The average metallicities $\langle Z_L \rangle$ and $\langle Z_M \rangle$ can be derived similarly.

6.1.1 SFH via STARLIGHT Fitting

As illustrated by Cid Fernandes et al. (2005), the individual output vector may be dramatically deviated from the simulated input value. However, the average values of stellar age and metallicity should be more reliable, whatever they are weighted by light or mass. The flux-weighted age is more sensitive to the young stellar component, so the mass-weighted age is more underlying and intrinsic. The situation is the same for average metallicity. In this section, we will take the average ages and metallicities weighted by stellar mass. Since stellar population in ETGs are dominated by the old components, the ETGs have their average ages within a relatively narrow range.

Figure 10 presents the derived mass-weighted ages and metallicities as functions of cluster-centric radius R and total stellar mass (M_*) assembled in cluster galaxies. The upper two panels show the mass-weighted ages and metallicities as a function of R . The galaxies in the core region ($R < 400$ kpc) of A671 are denoted by filled symbols. The remarkable morphology-density segregation of A671 is well shown in these two panels. The LTGs (denote by blue symbols) locate in the outskirts (denoted by open symbols), and have younger stellar ages. On the other hand, the ETGs with older stellar ages are located in the core region. For the ETGs of A671, no correlation is found between metallicities and R .

The lower two panels of Figure 10 present how the mass-weighted ages and metallicities correlate with stellar mass. Both ages and metallicities are found to be correlated strongly with stellar mass, and such correlations are dependent upon morphology. In general, the more massive galaxies have older ages and richer metallicities. For the LTGs in A671, the linear correlations of age and metallicity with stellar mass appear tighter and steeper. Even for the ETGs with similar stellar mass, the ETGs in core region tend to have older ages than the outskirt ETGs. However, the ETG metallicities seem to not vary with cluster-centric radius.

6.2 Lick Indices

The age-metallicity degeneracy has haunted stellar population analysis for decades. Nevertheless, the promising approach to break it remains the combined use of multiple absorption-line indices (Kong & Cheng 2001). In this section, we will measure the absorption lines of ETGs in A671 and compare them with state-of-art SSP models in order to infer their ages, metallicities and α -enhancements.

6.2.1 Lick Index Measurements

The bandpasses of the Lick indices are defined in Table 1 of Worthey et al. (1994). We measure the Lick indices with a mod-

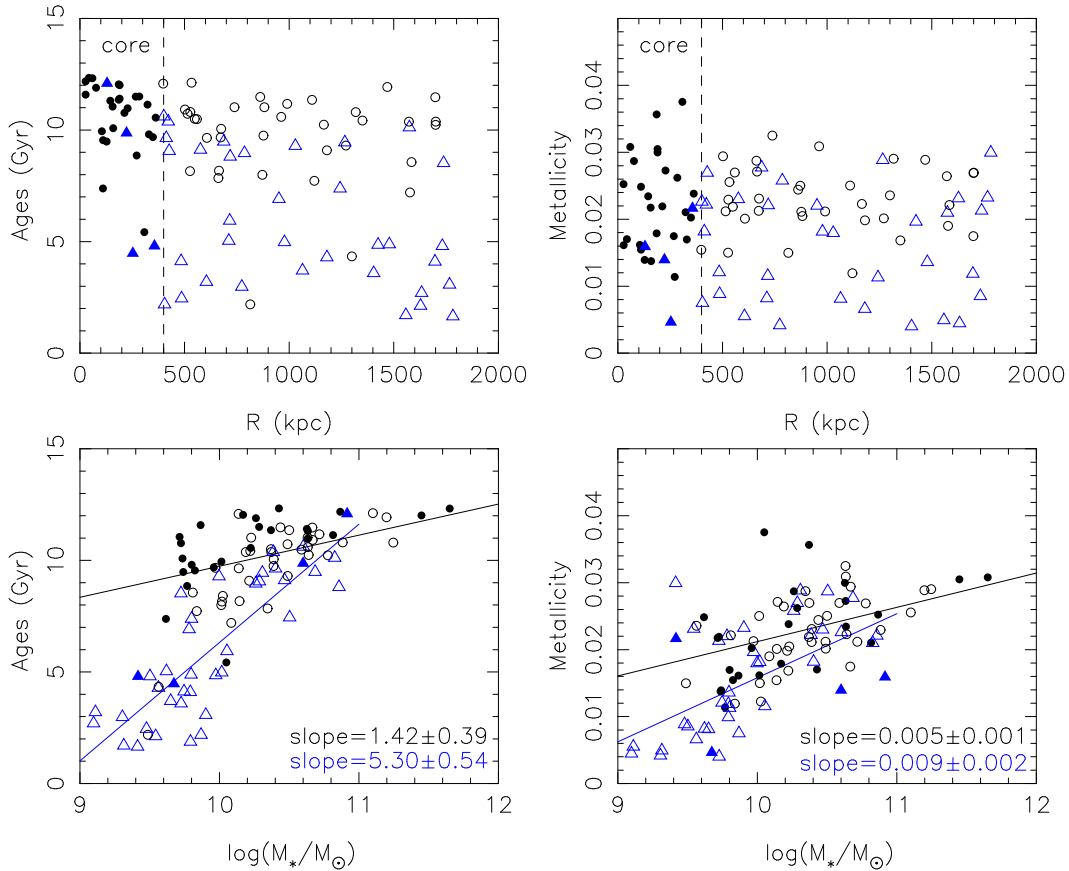


Figure 10. Correlation of mass-weighted ages and metallicities with cluster-centric radius R and stellar mass. Black circles represent the ETGs, while blue triangles represent the LTGs. Galaxies in the core region are denoted by filled symbols.

ified version of the Lick_EW routine in EZ_Ages package developed by Graves & Schiavon (2008)³. The Lick_EW routine reports the errors of each Lick index calculated in the way suggested by Cardiel et al. (1998). The SDSS spectral resolution (69 km s^{-1}) does not match the originally defined resolution of Lick indices. The Lick_EW routine smooths the SDSS spectra to the resolution of Lick/IDS system before measuring the indices. For the galaxies with high velocity dispersion, the smoothed absorption features in the SDSS spectra are at resolution even poorer than the Lick resolution, the Lick_EW routine will apply σ -correction for these galaxies. The output includes the measurements of σ -corrected indices and their errors.

One of the most challenging issues in Lick index measurements is emission line contamination. The Balmer absorption features are contaminated by emission from ionized gas, either from star formation, AGN activity or interstellar shocks. Balmer line emission was estimated from equivalent of $H\alpha$, which are retrieved from the MPA/JHU SDSS DR7 catalog. Some of previous studies used $\text{EW}(H\beta) = 0.6 \text{ EW}([\text{O III}]\lambda 5007)$ for correction (Trager et al. 2000). We do not use $[\text{O III}]\lambda 5007$ for correction because Nelan et al. (2005) have found that the relation between $H\beta$ and $[\text{O III}]\lambda 5007$ for the ETGs varies in different mass ranges. They found that the correlation between $H\beta$ and $H\alpha$ is much tighter. Emission EWs for higher order Balmer lines are obtained from $H\alpha$ by assuming standard values from Balmer decrement (in the

absence of reddening). In this way, $\text{EW}(H\beta) = 0.36 \text{ EW}(H\alpha)$, $\text{EW}(H\gamma) = 0.19 \text{ EW}(H\alpha)$, and $\text{EW}(H\delta) = 0.13 \text{ EW}(H\alpha)$.

6.2.2 SSP Model and Stellar Population Parameters

Our goal is to use the S07 model to derive the SSP-equivalent parameters. Firstly we create grid to fit three parameters: ages, $[\text{Fe}/\text{H}]$, and $[\text{Mg}/\text{Fe}]$. We use the solar-scaled isochrones and the Salpeter initial mass function suggested by the EZ_Ages documents. The $[\text{O}/\text{Fe}]$ is set to be zero, and other α elements are tied to Mg. The ages range from 1.2 to 17.7 Gyr, and the $[\text{Fe}/\text{H}]$ ranges from -1.3 to 0.2. Other details can be found in S07, Graves & Schiavon (2008).

The three parameters are derived following two steps: i) for each galaxy, we firstly calculate age and $[\text{Fe}/\text{H}]$ using $H\beta$ and $\langle \text{Fe} \rangle$, at all $[\text{Mg}/\text{Fe}]$; ii) we compare the pair $\langle \text{Fe} \rangle$ ($\langle \text{Fe} \rangle = 0.5(\text{Fe}5270 + \text{Fe}5335)$) and Mgb with models at the median age obtained in the first step, and calculate a new $[\text{Fe}/\text{H}]$ and $[\text{Mg}/\text{Fe}]$. We then update the ages by interpolating the ages found in the first step at the $[\text{Mg}/\text{Fe}]$ derived in the second step, and iterate the second step with the new age. Usually two iteration steps are needed before convergence. For those measurements beyond the model grids, we set the parameters to be the boundaries, i.e., the maximum or minimum of the models.

Before deriving the stellar population parameters of our sample with the SSP models, we compare our measurements to the predictions of each model on the grids of age and metallicity. In Figure 11, our measurements of $H\beta$ and $[\text{Mg}/\text{Fe}]'$ are compared with the

³ http://www.ucolick.org/~graves/EZ_Ages.html

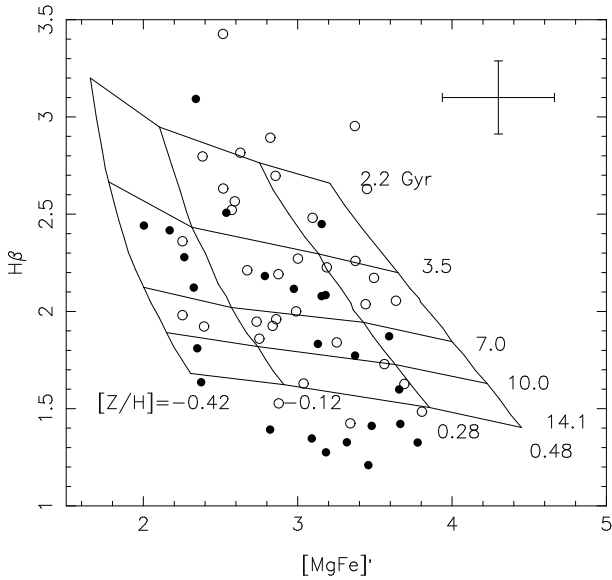


Figure 11. The index plot on the S07 model grid assuming $[\alpha/\text{Fe}]=0.2$, shows the $[\text{MgFe}]'$ vs. $H\beta$. The filled and open circles represent the ETGs in the core region and those in outskirts, respectively.

S07 models assuming $[\alpha/\text{Fe}]=0.2$, where the index $[\text{MgFe}]'$ is defined as follows: $[\text{MgFe}]' = \sqrt{\text{Mgb}(0.72\text{Fe}5270 + 0.28\text{Fe}5335)}$. $[\text{MgFe}]'$ is a good indicator of metallicity which is almost independent upon α/Fe ration variations (Thomas et al. 2003) (hereafter TMB). To convert between $[\text{Fe}/\text{H}]$ and $[\text{Z}/\text{H}]$, we adopt the relation given by TMB: $[\text{Z}/\text{H}] = [\text{Fe}/\text{H}] + 0.94[\alpha/\text{Fe}]$, and we assume $[\text{Mg}/\text{Fe}] = [\alpha/\text{Fe}]$. The median age is about 7 Gyr but with a large scatter. Most of the core-region galaxies have very small $H\beta$ values, and occupy the oldest end of age distribution. The $[\text{MgFe}]'$ is mainly distributed along $[\text{Z}/\text{H}] = 0$, and does not have any environmental effects.

We present the derived six SSP parameters as a function of velocity dispersion (σ) in Figure 12. Galaxies which fall outside model boundary are not included in the figure. The parameter errors are given by the fitting procedure for each galaxy. We then compute an average error for each parameter by weighted the output error of individual galaxy with its signal-to-noise ratio. As presented in Figure 11, majority of the galaxies falling out of the model boundary are located in the core, which makes hard to investigate environmental effect. Though only 46 ETGs are able to be fitted by the model, the relations between the SSP parameters and velocity dispersion (σ) are still remarkable.

In the top-left panel of Figure 12, the SSP ages show strong dependence upon velocity dispersion, and the low- σ galaxies span a wider age range, indicating that the low σ galaxies have various possibilities of star formation histories compared with the high- σ ones. Similar results are found in the bright galaxies in Coma by Price et al. (2011). It is noteworthy that the SSP ages derived by S07 model are not compatible with the average stellar ages given by the STARLIGHT fitting. Firstly, the SSP ages in STARLIGHT code range from 1 Myr to 13 Gyr, while the range of the SSP ages in S07 models is from 1 Gyr to 17.7 Gyr. The typical age of ETGs from STARLIGHT fitting (see Figure 10) is older than 7 Gyr. In Figure 11, the ETG ages derived by the S07 model span a wider range. Additionally, the STARLIGHT gives the best-fit ages without errors. The S07 model determines the ages by comparing several combined-indices with the theoretical model, and the measure-

ment errors can strongly affect the output ages. For the galaxies whose indices locate near the model boundary, measurement errors of indices will bring in greater uncertainties in the parameter fitting.

The top-middle and top-right panels display the relation of $[\text{Fe}/\text{H}]$ and $[\text{Mg}/\text{Fe}]$ with σ . The $[\text{Fe}/\text{H}]-\sigma$ correlation is very tight, with a correlation coefficient of $r_s = 0.513$, whereas the $[\text{Mg}/\text{Fe}]-\sigma$ correlation is rather weak. The former studies have found $[\text{Mg}/\text{Fe}]$ strongly correlated with σ (Thomas et al. 2005; Zhu et al. 2010). We should keep in mind that the tightness and slope of linear correlation strongly depend on the sample size. Considering our small sample size and the intrinsic scatter of this correlation, a relatively weaker $[\text{Mg}/\text{Fe}]-\sigma$ relation is still reasonable.

In the three bottom panels of Figure 12, we present $[\text{C}/\text{Fe}]-\sigma$, $[\text{N}/\text{Fe}]-\sigma$, and $[\text{Ca}/\text{Fe}]-\sigma$ relations. Only a weak correlation of $[\text{N}/\text{Fe}]-\sigma$ is found, with a correlation coefficient of $r_s = 0.404$. The results of our fitting are similar to those in Graves et al. (2008), and their results are based on a large sample of about 6000 red sequence galaxies from the SDSS.

7 DISCUSSION

We have investigated the dynamics of A671 based on the spectroscopically confirmed members, and the result of κ -test strongly suggests that A671 has significant substructures. Many authors have found that a large fraction of galaxy clusters have substructures (Dressler 1988; Mohr et al. 1993; Yuan et al. 2003; Yang et al. 2004), indicating that massive clusters may assemble their masses and grow up by accreting small groups. The contour map of member galaxies in A671 fits well with the X-ray intensity contour map. Ramella et al. (2007) suggested that there are two substructures in A671. Location of one substructure is well associated with the potential substructure B, and the other is at the south part of cluster, which is not significant enough to be detected by the κ -test. Their substructure-finding algorithm is based on the projected positions of galaxies, and does not utilize the redshift information. 73% of the clusters in their sample were found to have substructures, and this fraction is higher than most studies. Their magnitude limit of galaxy samples is $V \simeq 21^m.2$, much fainter than our limiting magnitude $h_{\text{BATC}} = 19^m.5$, thus the projection effect cannot be ignored, and some substructures they found could be untrue. After 97 newly selected galaxies included, the substructure B is enhanced, while another substructure appears less prominent. The follow-up spectroscopy of these faint galaxies is need for revealing the details of dynamical substructures in A671.

The remarkable morphology-density relation indicates that the cluster environment indeed have played an important role in evolution of cluster galaxies. A visual inspection of the C-M diagram shows that a large fraction of bright member galaxies ($h_{\text{BATC}} < 18^m.5$) have evolved to be the ‘‘red sequence’’, and faint member galaxies with $h_{\text{BATC}} \sim 19^m.0$ are found to have considerable activities of star formation. When the galaxies are accreted into a cluster, their star formation activities are expected to be suppressed by some important processes, such as tidal stripping and ‘‘harassment’’ (Moore et al. 1996), ram pressure stripping of the gas disk (Abadi et al. 1999), and removal of gas reservoir surrounding each galaxy (Balogh et al. 2002).

We derived the average ages and metallicities for member galaxies by fitting their spectra. The most remarkable feature of the age distribution is that the ETGs in the core region have older ages than those in the outskirts. Thomas et al. (2005) have found that the ETGs in dense environment have average ages ~ 2 Gyr older

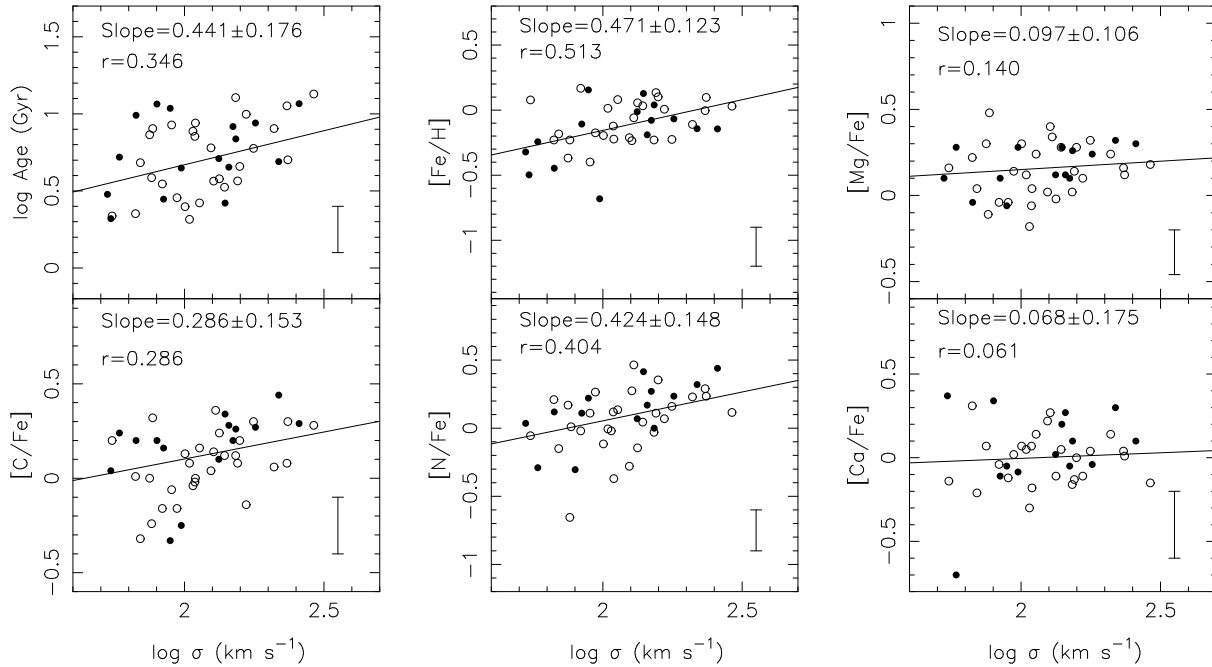


Figure 12. The six SSP-equivalent parameters as the functions of velocity dispersion σ for the 46 galaxies which can be fitted by the models. The symbols are defined in Figure 10. The black line represents the linear fit.

than those in field environment. They derived ages by comparing the Lick indices with the prediction of TMB model. Our results confirm their conclusion though the average ages are derived by different methods. This can be interpreted in two ways. On the one hand, theoretical work shows that dark matter halos in dense environments were assembled earlier than average (Gao et al. 2005). As a result, the galaxies in the core region of clusters formed earlier than those in the outer regions, and thus have older stellar ages. On the other hand, the older stellar age of the ETGs in the core region could be explained by lack of recent star formation compared with those in the outer region. Galaxy clusters have dense gas with high temperature, and the core-region galaxies lost their gas reservoirs by interacting with the dense intracluster medium (ICM) (usually by ram pressure stripping). Thus the core-region galaxies should be gas-poor, and have less possibilities of recent star-formation. Aside from age, the total metallicities of the ETGs show subtle dependence on environment, which agrees well with Zhu et al. (2010). A larger sample of cluster ETGs is needed to investigate the environmental effects on chemical evolution.

The dependence of age upon stellar mass could be explainable in the downsizing scenario for galaxy formation (Cowie et al. 1996). In this scenario, star formation lasts longer in less massive galaxies than in more massive galaxies. Thus massive systems will have older SSP ages on average. Evidences of downsizing effect in the local universe have been found by many recent studies on the stellar population of ETGs (Nelán et al. 2005; Graves et al. 2008; Zhu et al. 2010; Price et al. 2011). The age- σ slope in these studies span a range between 0.35 and 0.93. The different slope values are mainly due to the different sample property (e.g., galaxy type, sample size, etc.) and methods of index correction (e.g., emission infill correction, velocity dispersion correction, etc.). Price et al. (2011) have tested the robustness of their observed age- σ slope against these two factors when they studied the stellar population in Coma. In their test, a stricter emission-line cut and different methods of velocity dispersion correction were used. Only slight change on the

age- σ slope was found in their tests. They concluded that their data robustly support the downsizing scenario.

The ETGs also have very strong dependence of α -abundance on σ . The α elements are mainly from the Type II supernovae, and the iron-peak elements come mainly from the Type Ia supernovae. The stronger alpha-enhancement in the more massive elliptical galaxies may imply that their star formation timescale is shorter than less massive elliptical galaxies, before the delayed Type Ia supernovae enrich the star-forming regions with iron-peak elements. The observed α -abundance- σ relation fits well with the prediction from the hierarchical models with feedback (De Lucia et al. 2006).

8 CONCLUSION

This paper presents a photometric study of A671 with the Beijing-Arizona-Taiwan-Connecticut (BATC) multicolor system and the SDSS data. The main conclusions can be summarized as follow:

(i) About 7000 sources are detected in a BATC field of $58' \times 58'$ centered at A671, and their SEDs in 15 intermediate bands are obtained. The 985 galaxies brighter $h_{\text{BATC}} = 20^m.0$ are selected by cross-identifying our BATC source catalog with the released catalog of SDSS galaxies. There are 205 galaxies with known spectroscopic redshifts in our viewing field, among which 103 galaxies with $0.04 < z_{\text{sp}} < 0.06$ are selected as spectroscopically confirmed members of A671. The sample of bright member galaxies is composed of 63 ETGs and 40 LTGs.

(ii) The dynamics of A671 is investigated based on the 103 spectroscopically confirmed members. The result of κ -test on different scales strongly suggest that A671 have significant substructures. Three potential substructures have been suggested with the method of localized deviation of velocity distribution.

(iii) Photometric redshift technique is applied to the 985 galaxies for further membership determination. Our photometric redshifts (z_{ph}) of the bright members are basically consistent with the

spectroscopic redshifts (z_{sp}). Based on the statistics of photometric redshifts, the galaxies with $0.028 < z_{\text{ph}} < 0.073$ are selected as member candidates. After further selection by the color-magnitude relation, 97 galaxies down to $h_{\text{BATC}} = 19^m.5$ are picked up as faint members of A671.

(iv) Based on the enlarged sample of member galaxies, spatial distribution and velocity structure of A671 are studied. Since the large z_{ph} uncertainty of faint galaxies have smoothed the localized abnormality in velocity distribution, the κ -test of the enlarged sample does not confirm the three substructures mentioned above. The morphology-segregation becomes very remarkable after the faint members are taken into account. The luminosity function in the SDSS r-band shows a flat slope at faint end, $\alpha \sim -1.12$.

(v) Mass-weighted stellar ages and total metallicities of bright members are derived by fitting their spectra with the spectral synthesis code, STARLIGHT. The ETGs in the core region have older ages than those in the outskirts. The more massive ETGs are found to be older than the less massive ones. No environmental effect is found for the metallicities of the ETGs. Strong correlations of mean stellar age and metallicity with stellar mass are confirmed, and such correlations are found to be dependent upon morphology. The positive age-mass correlation supports the downsizing scenario.

(vi) A set of Lick indices of the ETGs is measured in order to derive their SSP-equivalent stellar parameters (such as age, [Fe/H], [Mg/Fe], [C/Fe], [N/Fe], and [Ca/Fe]) by utilizing S07 model. The ETGs at cluster center tend to have smaller $H\beta$ indices, indicating that central ETGs are likely to be older. The total metallicity indicator $[\text{MgFe}]'$ does not show any environmental effects. The relations between the six SSP-parameters and velocity dispersion (σ) are also studied. The relations between the SSP-parameters and σ in A671 are in good agreement with previous studies.

ACKNOWLEDGMENTS

This work was funded by the National Natural Science Foundation of China (NSFC) (Grant Nos. 10803007, 10873012, 10873016 and 11173016), the National Basic Research Program of China (973 Program) (Grant Nos. 2007CB815403, 2007CB815404), and the Chinese Universities Scientific Fund (CUSF). This research has made use of the NED, which is operated by the Jet Propulsion Laboratory, California Institute of Technology, under contract with the National Aeronautics and Space Administration.

We acknowledge the use of MPA/JAU Garching DR8 public data. We also thank Ricardo Schiavon and Genevieve J. Graves for making their codes and models publicly available.

Funding for the Sloan Digital Sky Survey (SDSS) has been provided by the Alfred P. Sloan Foundation, the Participating Institutions, the National Aeronautics and Space Administration, the National Science Foundation, the US Department of Energy, the Japanese Monbukagakusho and the Max-Planck Society. The SDSS web site is <http://www.sdss.org>.

The SDSS is managed by the Astrophysical Research Consortium for the participating Institutions. The Participating Institutions are the University of Chicago, Fermilab, the Institute for Advanced Study, the Japan Participation Group, Los Alamos National Laboratory, the Max-Planck Institute for Astronomy (MPIA), New Mexico State University, University of Pittsburgh, University of Portsmouth, Princeton University, the United States Naval Observatory and the University of Washington.

REFERENCES

- Abadi M. G., Moore B., & Bower R. G., 1999, MNRAS, 308, 947
 Abell G. O., 1958, ApJS, 3, 211
 Aguerri J. A. L., Sánchez-Janssen R., & Muñoz-Tuñón, 2007, A&A, 471, 17
 Allen D. A., 1976, MNRAS, 174, 29
 Baldry I. K., Balogh R. G., Bower K., Glazebrook K., Nichol R. C., Bamford S. P., & Budavari T., 2006, MNRAS, 373, 469
 Balogh M. L., et al., 2002, MNRAS, 335, 10
 Bautz L. P., & Morgan, W. W., 1970, ApJL, 162, L149
 Beers T. C., Flynn K., & Gebhart K., 1990, AJ, 100, 32
 Beers T. C., Gebhardt K., Forman W., Huchra J. P., Jones C., 1991, AJ, 102, 1581
 Beijersbergen M., Hoekstra H., van Dokkum P. G., & van de Hulst T., 2002, MNRAS, 329, 385
 Bertin E. & Arnouts S., 1996, A&A, 117, 393
 Bolzonella M., Miralles J. M., & Pelló R., 2000, A&A, 363, 476
 Bower R. G., Lucey J. R., & Ellis R. S., 1992, MNRAS, 254, 589
 Blanton M. R. et al., 2003, ApJ, 592, 819
 Bruzual G., Charlot S., 2003, MNRAS, 344, 1000
 Butcher H. & Oemler A. Jr., 1978, ApJ, 226, 559
 Cardelli J. A., Clayton G. C., Mathis J. S., 1989, ApJ, 345, 245
 Cardiel N., Gorgas J., Cenarro J., & Gonzalez J. J., 1998, A&AS, 127, 597
 Carlberg R. G., Yee H. K. C., & Ellingson E., 1997, ApJ, 478, 462
 Cid Fernandes R., Mateus A., Sodré, L., Stasińska G., Gomes J. M., 2005, MNRAS, 358, 363
 Cid Fernandes R., Asari N. V., Sodré, L., Stasińska G., Mateus A. et al., 2007, MNRAS, 375, L16
 Colberg J. M., White S. D. M. et al., 2000, MNRAS, 319, 209
 Colless M., & Dunn A. M., 1996, ApJ, 458, 435
 Crone M. M., Evrard A. E., & Richstone D. O., 1996, ApJ, 467, 489
 Cowie L. L., Songaila A., Hu E. M., & Cohen J. G., 1996, AJ, 112, 839
 De Lucia G., Springel V., White S. D. M., Croton D., & Kauffmann G. 2006, MNRAS, 366, 499
 de Filippis E., Paolillo M., Longo G., La Barbera F., de Carvalho R. R., Gal R., 2011, MNRAS, 414, 2771
 Dessler A., 1980, ApJ, 236, 351
 Dessler A., Oemler A. Jr. et al., 1997, ApJ, 490, 577
 Dressler A. & Shectman S. A., 1988, AJ, 95, 985
 Ebeling H., Edge A. C., Böhringer H., Allen S. W., Crawford C. S., Fabian A. C., Voges W., Huchra J. P., 1998, MNRAS, 301, 881
 Fan X., Burstein D., Chen J. S. et al., 1996, AJ, 112, 628
 Fasano G., Poggianti B. M., Couch W. J., Bettoni D. et al., 2000, ApJ, 542, 673
 Fernández-Soto A., Lanzetta K. M., Yahil A., 1999, ApJ, 513, 34
 Gómez P. L., Nichol R. C., Miller C. J. et al., 2003, ApJ, 584, 210
 Gao L., Springel V. & White S. D. M., 2005, MNRAS, 363, L66
 Geller M. J. & Peebles P. J. E., 1973, ApJ, 184, 329
 Gott J. R. I., 1972, ApJ, 173, 277
 Goto T., Tamauchi C., Fujita Y., Okamura S. et al., 2003, MNRAS, 346, 601
 Graves G. J., Faber S. M., Schiavon R. P., Yan R., 2007, ApJ, 671, 243
 Graves G. J., & Schiavon R. P., 2008, ApJS, 177, 446
 Gunn J. E., & Stryker L. L., 1983, ApJS, 52, 121
 Hansen S. M., McKay T. A., Wechsler R. H., Annis J., Sheldon E. S., & Kimball A., 2005, ApJ, 633, 122

- Holden B. P., Illingworth G. D., Franx M., Blakeslee J. P. et al., 2007, *ApJ*, 670, 190
- Ilbert O., Capak P., Salvato M. et al., 2009, *ApJ*, 690, 1236
- Jones C. & Forman W., 1999, *ApJ*, 511, 65
- Kauffmann G., White S. D. M., Heckman T. M. et al., 2004, *MNRAS*, 353, 713
- Kong X., et al., 2000, *AJ*, 119, 2745
- Kong X., & Cheng F.Z., 2001, *MNRAS*, 323, 1035
- Kong X., Fang G., Arimoto N., & Wang M. 2009, *ApJ*, 702, 1458
- Liu S. F., Yuan Q. R., Yang Y. B., Ma J., Jiang Z. J., Wu J. H., Wu Z. Y., Chen J. S. & Zhou X., 2011, *AJ*, 141, 99
- Mateus A., Sodré L., Cid Fernandes R. et al., 2006, *MNRAS*, 370, 721
- Mohr J. J., Fabricant D. G. & Geller M. J., 1993, *ApJ*, 413, 492
- Moore B., Katz N., Lake G., Dressler A., & Oemler A., 1996, *Nature*, 379, 613
- Muratov A. L. & Gnedin O. Y., 2010, *ApJ*, 718, 1266
- Nelan J. E., Smith R. J., Hudson M. J., Wegner G. A., Lucey J. R. et al., 2005, *ApJ*, 632, 137
- Oegerle W. R., & Hill J. M., 1994, *AJ*, 107, 857
- Paollilo M., Andreon S., Longo G., Puddu E., Gal R. R., Scaramella R., Djorgovski S. G., de Carvalho R., 2001, *A&A*, 367, 59
- Postman M., & Geller M. J., 1984, *ApJ*, 281, 95
- Postman M. et al., 2005, *ApJ*, 623, 721P
- Price J., Phillipps S., Huxor A., Smith R. J. & Lucey J. R., 2011, *MNRAS*, 411, 2558
- Ramella M., Biviano A., Pisani A., Varela J., Bettoni D. et al., 2007, *A&A*, 470, 39
- Rhee G. F. R. N., van Haarlem M. P., Katgert P., 1991, *A&A*, 233, 325
- Schiavon R. P., 2007, *ApJS*, 171, 146
- Schechter P., 1976, *ApJ*, 203, 297
- Schuecker P., Böhringer H., Reiprich T. H., & Feretti L., 2001 *A&A*, 378, 408
- Smith G. P., Treu T., Ellis R. S., Moran S. M., Dressler A., 2005, *ApJ*, 620, 78S
- Thomas P. A. et al., 1998, *MNRAS*, 296, 1061
- Thomas D., Maraston C. & Bender R., 2003, *MNRAS*, 339, 897
- Thomas D., Maraston C., Bender R., Mendes de Oliveira C., 2005, *ApJ*, 621, 673
- Trager S. C., Faber S. M., Worthey G. & González J. J., 2000, *AJ*, 119, 1645
- West M. J., Villumsen J. V., Dekel A., 1991, *ApJ*, 369, 287
- West M. J., Jones C., Forman W., 1995, *ApJ*, 451, L5
- Whitmore B. C. & Gilmore D. M., 1991, *ApJ*, 367, 64W
- Worthey G., Faber S. M., Gonzalez J. J. & Burstein D., 1994, *ApJS*, 94, 687
- Xia L. F., Zhou X., Ma J., et al., 2002, *PASP*, 114, 1349
- Yang Y. B., Zhou X., Yuan Q. R., Jiang Z. J., Ma J., Wu H., Chen, J. S., 2004, *ApJ*, 600, 141
- Yuan Q. R., Zhou X., Jiang Z. J., 2003, *ApJS*, 149, 53
- Yuan Q. R., Zhou X., Chen J. S., Ma J., Wu H., Xue S. J., Zhu J., 2001, *AJ*, 122, 1718
- Zhang L., Yuan Q. R., Yang Q., et al., 2011, *PASJ*, 63, 585
- Zhou X., Chen J. S., Xu W. et al., 1999, *PASP*, 111, 909
- Zhou X., Jiang Z. J., Xue S. J., Wu H., Ma J., Chen J. S., 2001, *ChJAA*, 1, 372
- Zhu G. T., Blanton M. R. & Moustakas J., 2010, *ApJ*, 722, 491